



UNIVERSITY OF LEEDS

This is a repository copy of *An experimental and numerical investigation of CO₂ corrosion in a rapid expansion pipe geometry*.

White Rose Research Online URL for this paper:
<http://eprints.whiterose.ac.uk/154070/>

Version: Accepted Version

Article:

Owen, J orcid.org/0000-0003-0778-0858, Godfrey, J, Ma, W et al. (6 more authors) (2020) An experimental and numerical investigation of CO₂ corrosion in a rapid expansion pipe geometry. *Corrosion Science*, 165. 108362. ISSN 0010-938X

<https://doi.org/10.1016/j.corsci.2019.108362>

© 2019 Elsevier Ltd. All rights reserved. This manuscript version is made available under the CC-BY-NC-ND 4.0 license <http://creativecommons.org/licenses/by-nc-nd/4.0/>.

Reuse

This article is distributed under the terms of the Creative Commons Attribution-NonCommercial-NoDerivs (CC BY-NC-ND) licence. This licence only allows you to download this work and share it with others as long as you credit the authors, but you can't change the article in any way or use it commercially. More information and the full terms of the licence here: <https://creativecommons.org/licenses/>

Takedown

If you consider content in White Rose Research Online to be in breach of UK law, please notify us by emailing eprints@whiterose.ac.uk including the URL of the record and the reason for the withdrawal request.



eprints@whiterose.ac.uk
<https://eprints.whiterose.ac.uk/>

An experimental and numerical investigation of CO₂ corrosion in a rapid expansion pipe geometry

Joshua Owen^a, Jack Godfrey^a, Wenlong Ma^{a,b}, Greg de Boer^a, Mohammed Al-Khateeb^a, Harvey Thompson^a, Anne Neville^a, Callum Ramsey^c and Richard Barker^a

^a *School of Mechanical Engineering, University of Leeds, Leeds, LS2 9JT, United Kingdom*

^b *School of Mechanical and Electronic Engineering, China University of Petroleum, Qingdao 266580, P.R. China*

^c *Shell U.K. Limited, 1 Altens Farm Road, Nigg, Aberdeen, AB12 3FY, United Kingdom*

Abstract

A combined experimental and numerical methodology for accurately translating Rotating Cylinder Electrode (RCE) CO₂ corrosion data to complex pipe flow geometries is presented. Computational Fluid Dynamics (CFD) simulations are used to determine the local variation in mass-transfer coefficient throughout a rapid expansion (as an example geometry). An empirical correlation between mass-transfer coefficient and corrosion rate derived from RCE experiments is then integrated into the CFD model to predict the variation in corrosion rate throughout the fitting. Electrochemical and mass loss corrosion experiments using carbon steel coupons integrated into a 3D printed rapid expansion within a flow loop validate the approach.

Keywords

Flow-induced CO₂ corrosion, empirical corrosion model, mass transfer, computational fluid dynamics, X65 carbon steel

1. Introduction

Flow-induced corrosion of carbon steel pipelines in carbon dioxide (CO₂)-saturated environments can be severe within the oil and gas industry, with high degradation rates causing leakages, resulting in down-time, financial implications and risk to the environment. A wide range of environmental conditions are known to influence the corrosion rate of carbon steel in CO₂-saturated environments, including partial pressure of CO₂, temperature and pH [1]. One of the most influential factors determining corrosion

rates of carbon steel is fluid flow, which has been the subject of several investigations [2-6]. In the absence of protective surface films, the primary effect of flow is to enhance mass transfer of species involved in the corrosion reaction at the metal surface. In instances where the electrochemical processes at the steel surface occur faster than electrochemically active species can be transported from the bulk solution to the surface, the system is said to be mass transfer controlled. In this scenario, a change in flow rate will influence the reaction rate. However, if the corrosion process is governed by charge-transfer (activation controlled), changes in the flow rate will have zero, or minimal, effect on the corrosion rate [2].

When CO₂ dissolves into an aqueous solution, the formation of carbonic acid is permitted. The dissociation of carbonic acid provides a source of hydrogen ions (H⁺), which are subsequently reduced at the steel surface:



The role of carbonic acid in the cathodic reaction has been widely debated since it was initially discussed by de Waard and Milliams [7], who proposed that direct reduction of carbonic acid at the steel surface provided an additional cathodic reaction. However, it was more recently suggested that the direct reduction of carbonic acid does not occur to any significant effect, but instead dissociates near to the steel surface, providing additional H⁺ ions, which are subsequently reduced in a process now referred to as the 'buffering effect' [8, 9]. Subsequent experimental evidence for the 'buffering effect', suggesting zero or minimal contribution from direct reduction of carbonic acid, has now been provided across a range of conditions [10-13].

In relation to Equation (1), the rate at which this reaction proceeds on a carbon steel surface in a CO₂-containing environment can be significantly influenced by both hydrodynamics and pH. At pH < 4 (referred to as 'low pH' in this study), it has been shown that the rate limiting step associated with H⁺ reduction can be the diffusion rate from the bulk solution to the steel surface [2, 14]. In the pH range of 4 to 6, the role of carbonic acid in the cathodic reaction becomes more significant [11, 15, 16], whilst rate-limiting steps associated with this are less dependent on flow, particularly as pH increases [1]. However, some sensitivity to flow has been observed and has subsequently been accounted for in recent mechanistic models [17, 18]. Consequently, understanding the

relationship between fluid flow characteristics and the rates of the aforementioned reaction is important when interpreting the mechanism of CO₂ corrosion and predicting corrosion rates observed in the field.

The anodic reaction, electrochemical dissolution of iron, can be summarised using Equation (2).



However, it should be noted that the dissolution of iron consists of a series of reactions involving the generation and consumption of various intermediate products prior to the production of an iron ion [1, 15, 19].

1.1. Prediction of CO₂ Corrosion Rates in the Field

With the exception of running large-scale flow loop studies under the exact hydrodynamic regime as those encountered in oil and gas production, two main methods exist by which CO₂ corrosion rates can be predicted in the field. These are:

- i. translation of laboratory-based results to the field using scaling parameters to account for the differences in system geometry
- ii. development of mathematical models to predict corrosion rates in pipeline geometries

1.1.1. Translation of Laboratory-Based Results to the Field

Several hydrodynamic parameters have been explored across various system geometries in experimental investigations of flow-induced corrosion. The most commonly used parameters are shear stress [4, 6, 20] and mass transfer coefficient [2, 21]. The corrosion rate dependence on basic flow parameters, such as flow velocity and Reynolds number, which are often reported, cannot be easily translated from one geometry to another, or subsequently the field in a CO₂ corrosion scenario, due to the geometry-specific nature of the parameters. The processes occurring in such systems are so complicated that a single scaling parameter such as Reynolds number, shear stress, turbulent intensity etc. is unlikely to exist.

The translation of data from one system geometry to another to predict what will occur in the field is therefore particularly challenging. That being said, the use of the mass

transfer coefficient as a hydrodynamic parameter has been shown to provide correlations with CO₂ corrosion rates which are generally translatable to different system geometries (i.e. a geometry independent parameter) for corrosion in the absence of protective corrosion product layers [22-24]. This is shown in research by Nešić et al. [2] where a comparison between two flow geometries (the Rotating Cylinder Electrode (RCE) and straight pipe flow) was carried out in terms of hydrodynamics, mass transfer, and CO₂ corrosion rates. In the case of CO₂ corrosion, Nešić et al. [2] showed it was possible to achieve a strong agreement between corrosion rates in the two flow geometries at low temperatures by reproducing the same water chemistry and mass transfer coefficient. This confirmed that in the absence of surface films, the use of mass transfer coefficients facilitates transfer of data from one flow system to another, and ultimately to the field.

1.1.2. Mechanistic CO₂ Corrosion Models for Corrosion Rate Predictions

From a mechanistic modelling perspective, corrosion rates are often determined using fundamentals of charge-transfer, chemical processes and mass transfer processes [25]. Recent mechanistic models [17, 18] predict corrosion rates by determining the concentration of electrochemically active species at the steel surface and bulk solution, relating the transport of the species from the bulk solution to the surface using mass transfer coefficients. Predictions made using these models compare well with experimental corrosion rates across a range of conditions in straight pipe and RCE flow geometries. However, these geometries have well-defined hydrodynamic conditions, meaning that mass transfer coefficients can be assumed to be constant over the entire steel surface throughout the geometry of interest.

Whilst the use of a single, and easily determined, mass transfer coefficient is appropriate for RCEs and straight pipes, more complex geometries have been shown to experience local variation in mass transfer coefficients [26, 27], and hence corrosion rates, limiting the applicability of models reliant on an input of a single mass transfer coefficient. Disturbances to the flow caused by such changes in flow geometry increase local turbulence and mass transfer, making components with abrupt changes in geometry more susceptible to high rates of corrosion than straight pipe flow in highly acidic CO₂ brines [27-29]. Complex flow geometries often do not have well-defined relationships for

determining mass transfer coefficients that can be universally applied and variation throughout the geometry prevents simple calculation of a single mass transfer coefficient.

1.2. Relevance and Importance of Accurate Mass Transfer Quantification

In terms of defining appropriate mass transfer coefficients, a handful of relationships exist in literature that can be used in specific geometries and conditions. For these relationships, the mass transfer coefficient is typically expressed in a function using the dimensionless Sherwood number, Sh [14]:

$$Sh = \frac{k_m L}{D_i} \quad (3)$$

where k_m is the mass transfer coefficient (m/s), D_i is the diffusion coefficient of species i (m^2/s) and L is a characteristic length (m). The numerator in Equation (3) represents the convective mass transfer of an ionic species and the denominator represents the rate of diffusion of the species. Empirical relationships, such as those proposed by Berger and Hau [30] and Eisenberg et al. [31], are used to calculate the mass transfer coefficient in straight pipes and RCEs, Equations (4) and (5), respectively:

$$Sh = 0.0165Re^{0.86}Sc^{0.33} \quad (4)$$

$$Sh = 0.0791Re^{0.7}Sc^{0.356} \quad (5)$$

where Re is the Reynolds number, $Re = \rho Ud/\mu$, where ρ is the fluid density (kg/m^3), d is the pipe diameter (m), U is the flow velocity (m/s), μ is the dynamic viscosity (Pa·s) and Sc is the Schmidt number, $Sc = \mu/\rho D$. The Eisenberg et al. [31] correlation has been reliably used to determine mass transfer coefficients in the RCE [23], producing excellent agreement in a previous study in similar environments to the conditions of interest in this study [32].

However, these relationships are only valid for certain conditions. For example, Equation (4) can only be used for smooth straight pipes with a Reynolds number up to 2×10^5 . There also remains a lack of correlations for conveniently determining mass transfer coefficients in complex pipe geometries, such as elbows, rapid expansions/contractions, plugged tees etc. Some exceptions to this statement include the work of Rizk et al. [26] and Wang et al. [27] who developed empirical relationships for predicting the maximum mass transfer coefficient in a rapid expansion and 90° pipe elbow respectively. However,

these equations enabled only a maximum mass transfer coefficient to be calculated and do not provide a method of determining local mass transfer coefficients throughout the entire geometry, which would provide greater detail about the corrosion rate variation throughout the geometry. These relationships are also only validated for a limited range of conditions and therefore cannot be generally applied.

There is, therefore, a requirement to bridge the gap between CO₂ corrosion models, which require a single mass transfer coefficient input to define the fluid flow regime, and the flow characteristics encountered in complex geometries. This would enable models to be developed which can assist in understanding and predicting corrosion rates in field geometries, where components are susceptible to corrosion, enabling better management and design. This study is concerned with modelling the influence of flow in a complex geometry on CO₂ corrosion of carbon steel in the absence of protective films in mass transfer-controlled environments. This work consists of several aspects: (i) the design of a novel 3D printed rapid expansion pipe flow component containing carbon steel coupons for simple laboratory-based corrosion experimentation in representative pipe flow conditions, (ii) development of a Computational Fluid Dynamics (CFD) model of the rapid expansion to simulate fluid flow and mass transfer in the geometry, (iii) generation of an empirical correlation between CO₂ corrosion rate and mass-transfer coefficient using an RCE, (iv) integration of the empirical correlation into CFD simulations of mass transfer to predict corrosion rates in the rapid expansion, validated experimentally using the newly-designed geometry. This study presents a significant enhancement of the current state-of-the-art for prediction of CO₂ corrosion rates by integrating CFD simulations of mass transfer into a CO₂ corrosion model, enabling predictions in more complex flow geometries with significant variations in local mass transfer coefficients.

2. Experimental Methodology

2.1. Rapid Expansion Component Design

A rapid expansion geometry was chosen for investigation of mass transfer and flow-induced corrosion, using a newly-designed 3D printed component, integrated into a flow loop. The fully assembled 3D model of the rapid expansion geometry is shown in Figure

1. An epoxy glue layer was applied around the inlet and outlet pipes when fitted into the flow loop.

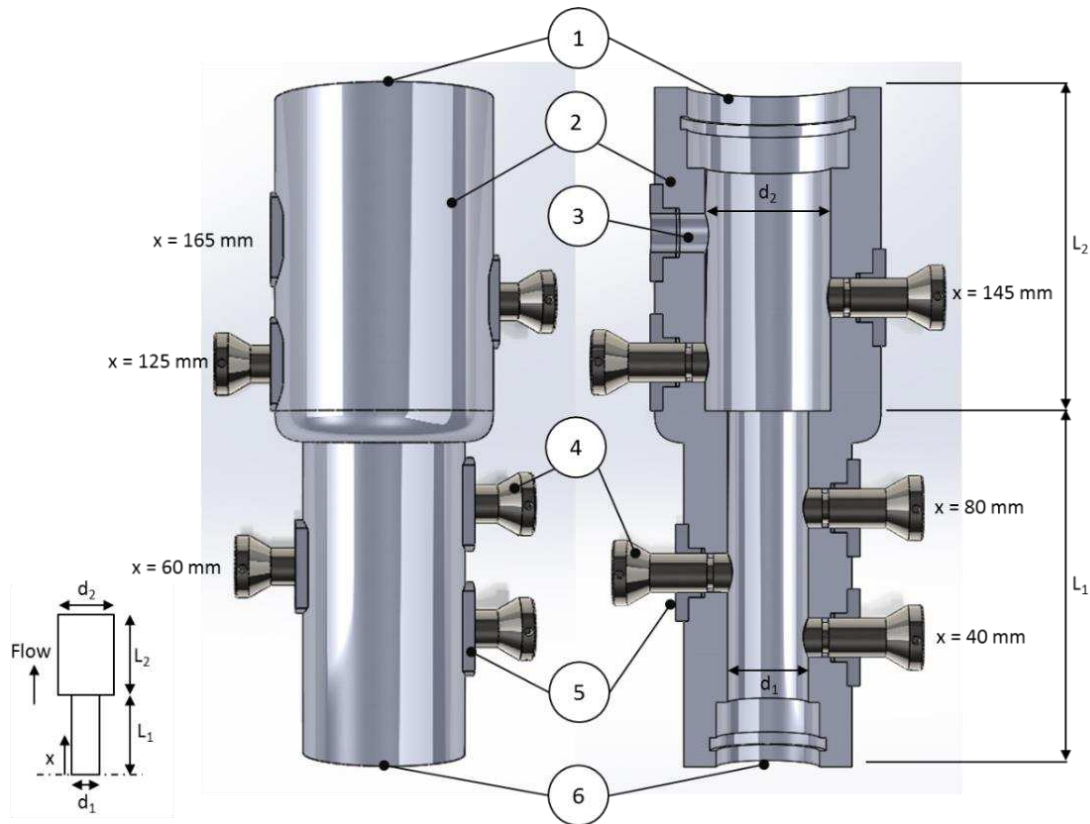


Figure 1: Fully assembled 3D model of rapid expansion pipe component design (rapid expansion 1 as named in Section 2.1) and cross-section through the centre of the component consisting of (1) flow outlet, (2) 3D printed body, (3) redox electrode positioned in the flow, (4) carbon steel coupons, (5) coupon holders and (6) flow inlet, where x is the distance to the centre of the coupon from the inlet, $d_1 = 25.4$ mm, $d_2 = 38.8$ mm, $L_1 = 110$ mm and $L_2 = 100$ mm. Two rapid expansion components were used with coupons located at different distances from the inlet. Coupons in rapid expansion 2 were positioned at $x = 60$ mm, 116 mm, 119 mm and 122 mm

Due to the size of the geometry and coupons used, it was more feasible to use two geometries containing multiple coupons. The two geometries used were:

- i. Rapid expansion 1, as shown in Figure 1, used for measurement of corrosion rates over a wide range of the expansion component. The coupons before the expansion were located at distances of 40 mm, 60 mm and 80 mm from the inlet, alternating on the pipe wall, and the coupons after the rapid expansion were located 125 mm and 145 mm from the inlet.

- ii. Rapid expansion 2, used for more detailed analysis of corrosion rates immediately after the expansion, with more coupons located in this particular region. A coupon was located before the expansion at a distance of 60 mm from the inlet (to confirm equivalence between both geometries). Coupons were positioned after the expansion at 116 mm, 119 mm and 122 mm from the inlet.

The expansion components were 3D printed using a material with similar properties to acrylonitrile-butadiene-styrene using a Stratasys Objet 1000 Plus 3D printer. Figure 2 shows how the rapid expansion geometry was integrated into the flow loop. The rapid expansion design and methodology for integration into a flow loop was based on the design of a 3D printed 90° elbow component, with a more detailed description of the methodology provided by Owen et al. [33]. The flow loop pipe work consisted of 25.4 mm inner diameter and 32 mm outer diameter chlorinated polyvinyl chloride (PVC-C) pipes before the expansion. PVC-C pipe with an inner diameter of 38.8 mm and outer diameter of 50 mm was used after the expansion before a reducing bush was used to decrease the flow diameter back to the 25.4 mm inner diameter pipes, approximately 10 internal diameters (d_2) after the expansion. The rapid expansion component was positioned at a distance of approximately 40 internal diameters (d_1) downstream of the pump, used to recirculate the solution through the flow loop, so that the flow could fully develop after exiting the pump. A minimum distance of 10 internal diameters is often required after flow disturbances to ensure flow has fully developed in turbulent pipe flow [34].

The coupon surface exposed to the flow was curved with the same radius as the internal radius of the flow channel, to prevent disturbance to the flow. Similar flush mounted coupons have been used successfully for electrochemical and gravimetric corrosion measurements in a straight pipe component [2]. Coupons could be fitted and removed from the components to complete mass loss measurements and determine degradation rates. To ensure coupons were flush mounted in the geometry, components of the same internal diameters of the rapid expansion could be inserted to push the coupons against. Coupons were also fitted into the body of the expansion at a known distance to verify internal alignment. Electrochemical measurements were completed by using the coupons as working electrodes as part of a three electrode cell. Carbon steel pins were inserted into the holes in the coupons to enable convenient connections to a potentiostat for

electrochemical measurements. Each test coupon had a surface area of $\sim 1.16 \text{ cm}^2$ exposed to the flow.

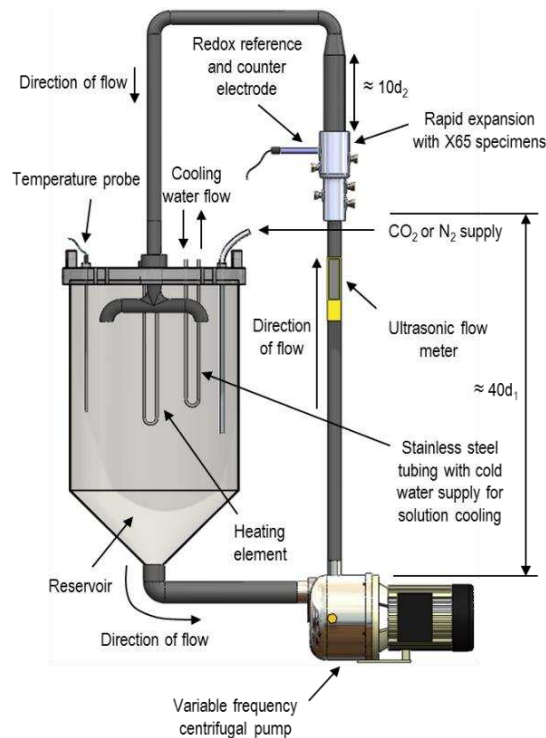


Figure 2: Flow loop containing the rapid expansion component, where d_1 is the inner diameter prior to the expansion and d_2 is the inner diameter after the expansion

2.2. Flow-Induced Corrosion

Flow-induced corrosion tests were completed to measure the corrosion rate of X65 carbon steel coupons, with the composition shown in Table 1. The coupon surfaces were ground by hand prior to testing using 320, 600, 800 and 1200 grit silicon carbide grinding paper to achieve a consistent surface finish across all coupons. Surface roughness has been shown to influence flow-induced corrosion rates and mass transfer coefficients [17, 32], however, coupons in this work were ground to a sufficiently low surface roughness to avoid such influences [35]. Therefore, the surface roughness was not expected to be a factor in terms of mass transfer and corrosion rate enhancement in this study. CO₂ was bubbled into the 50 L deionised water solution in the reservoir, containing 2% wt. sodium chloride (NaCl), for a minimum period of 12 h to reduce dissolved O₂ in the solution to less than 50 ppb (confirmed previously through the application of a colorimetric technique). After saturation, the solution pH was measured to be pH 3.7. The solution was

recirculated using the variable frequency pump at flow velocity of 2 m/s, measured at the inlet of the flow component using an ultrasonic flow meter (Micronics), positioned on the PVC-C pipes as shown in Figure 2. Tests were completed at solution temperature of 25°C, heated using a heating element and controlled to within $\pm 1^\circ\text{C}$ using a temperature controller, temperature probe and water cooling pipe, fitted into the flow loop reservoir as shown in Figure 2.

Table 1: X65 carbon steel composition (wt.%)

C	Mn	Ni	Nb	Mo	Si	V	P	S	Fe
0.15	1.422	0.09	0.054	0.17	0.22	0.06	0.025	0.002	97.81

Gravimetric measurements were used to determine the corrosion rates of each of the coupons, with this method being most appropriate for corrosion rate measurements in a steady-state environment with no film formation. Coupons were degreased with acetone, rinsed with distilled water and dried prior to measuring the mass of the coupon using a mass balance with a precision of ± 0.01 mg. The mass of the coupons was measured prior to, and after completing 4 h flow-induced corrosion tests to determine the mass loss of the X65 coupons. O-rings and coupon holders were removed from the coupons prior to completing mass loss measurements. To minimise crevice corrosion, a lacquer coating was applied to the sides of the coupons after initial measurement of the sample mass (m_1) and allowed to dry prior to inserting the coupons in the rapid expansion. This layer was removed using acetone after the tests and prior to measuring the mass of the sample (m_2). To determine corrosion rates from mass loss measurements in mm/year, the following equation was used:

$$V_c = \frac{87600\Delta m}{\rho_m A t} \quad (6)$$

where Δm is the mass loss of the coupon ($m_1 - m_2$) (g), ρ_m is the material density (g/cm^3), A is the surface area of the coupon (cm^2) and t is the test duration (h).

To demonstrate that corrosion rates were constant during a test, polarisation resistances (R_p) were measured *in-situ* and reported, with corrosion rates directly proportional to $1/R_p$. X65 coupons were used as working electrodes and connected to an ACM Gill 12-channel computer controlled potentiostat for electrochemical measurements. A

combination electrode, comprising of a silver/silver chloride (Ag/AgCl) reference electrode and a platinum (Pt) counter electrode, was used to complete the three electrode cell. Linear polarisation resistance (LPR) measurements were conducted by polarising the coupons from -15 mV to +15 mV relative to open circuit potential at a scan rate of 0.25 mV/s. LPR measurements were completed sequentially and on one coupon at a time to obtain polarisation resistances, with a total of 23 measurements performed on each coupon during 4 h.

2.3. Mass Transfer Coefficient Measurements

To measure mass transfer coefficients at each of the coupons, the 50 L, 2 wt.% NaCl, 25°C solution was saturated with nitrogen (N₂) and adjusted to pH 3 using dilute hydrochloric acid (HCl) to provide a source of H⁺ ions. N₂ was bubbled into the solution for a minimum period of 12 h. NaCl was added to the solution at the start of the bubbling period, and HCl was added after the solution was fully saturated with N₂, prior to the start of a test. Solution pH was measured using an automatic temperature compensation pH probe and monitored during the experiment. HCl was added whilst the solution was recirculating at a flow velocity of 2 m/s and pH was allowed to stabilise over a period of 0.5 h, to ensure equilibrium was reached throughout the 50 L solution, prior to starting electrochemical measurements. At low pH, in a deoxygenated environment, the only mass transfer controlled cathodic reaction that occurs is the reduction of H⁺ ions, Equation (1), where the mass transfer coefficient can be determined by measuring its associated limiting current, a technique that has been used reliably on several occasions [2, 14, 17]. The measurement of a limiting current allows mass transfer coefficient to be determined using Equation (7) [14, 22]:

$$Sh = \frac{i_{lim[H^+]}^d}{zF c_{b[H^+]}} \frac{L}{D_{[H^+]}} \quad (7)$$

where $i_{lim[H^+]}^d$ is the diffusion limited current of H⁺ ions (A/m²), z is the charge number (equal to 1 for H⁺ ions), F is the Faraday constant equal to 96,485 C/mol, and $c_{b[H^+]}$ is the bulk concentration of the ionic species (mol/m³), determined from the solution pH.

To obtain a limiting current, potentiodynamic cathodic sweeps were completed on each of the coupons, using the same three electrode setup used for flow-induced corrosion

tests. Cathodic sweeps were completed by polarising the X65 coupons from +15 mV above OCP to -1100 mV vs Ag/AgCl reference at a scan rate of 0.5 mV/s. OCP was allowed to stabilise prior to starting the measurements. Measurements were completed sequentially and lasted no longer than 0.5 h each, therefore mass transfer coefficients at the last coupon were obtained approximately 2 h after measurements at the first coupon. However, LPR measurements during flow-induced corrosion tests were completed to demonstrate that corrosion rate did not change substantially during the test in low pH, mass transfer-controlled conditions. To correct for solution resistance in cathodic potentiodynamic polarisation data, as a result of the geometrical distance between the working electrodes and combination electrode, the true applied potential was calculated by deducting the multiple of the solution resistance and measured current from the uncompensated potential, using Equation (8).

$$V = V_o - IR_s \quad (8)$$

where V_o is the uncompensated potential (V), I is the current density (A/cm^2) and R_s is the solution resistance ($\Omega \cdot cm^2$). To determine the solution resistance, electrochemical impedance spectroscopy measurements were completed over a frequency range from 20,000 Hz to 0.1 Hz.

2.4. Rotating Cylinder Electrode (RCE)

RCE experiments were completed at different rotational velocities to obtain an empirical correlation between mass transfer coefficient and corrosion rate, in the same experimental conditions as rapid expansion tests (2 wt.%, pH 3.7 and 25°C). Al Khateeb et al. [32] showed that corrosion rates in similar pH 4 conditions in the RCE were mass transfer controlled. A schematic of the RCE experimental setup is shown in Figure 3. Experiments were performed in a 1 L glass cell, saturated with CO₂ by bubbling gas into the solution for a period of 12 h prior to starting the experiment and throughout the duration of the 4 h tests. Experiments were conducted at rotational velocities ranging from 165 to 2700 RPM, to cover a range of mass transfer coefficients encompassing those predicted in the rapid expansion, detailed later in this study. The required range of rotational rates of the RCE shaft were determined using the Eisenberg et al. [31] correlation, Equation (5). To determine corrosion rates of X65 carbon steel samples, mass loss measurements of the samples were performed before and after the 4 h tests. Samples

were progressively wet-ground prior to testing using 320, 600, 800 and 1200 grit silicon carbide grinding paper. After grinding, samples were degreased with acetone, rinsed with distilled water and dried prior to weighing using a mass balance with a precision of ± 0.01 mg.

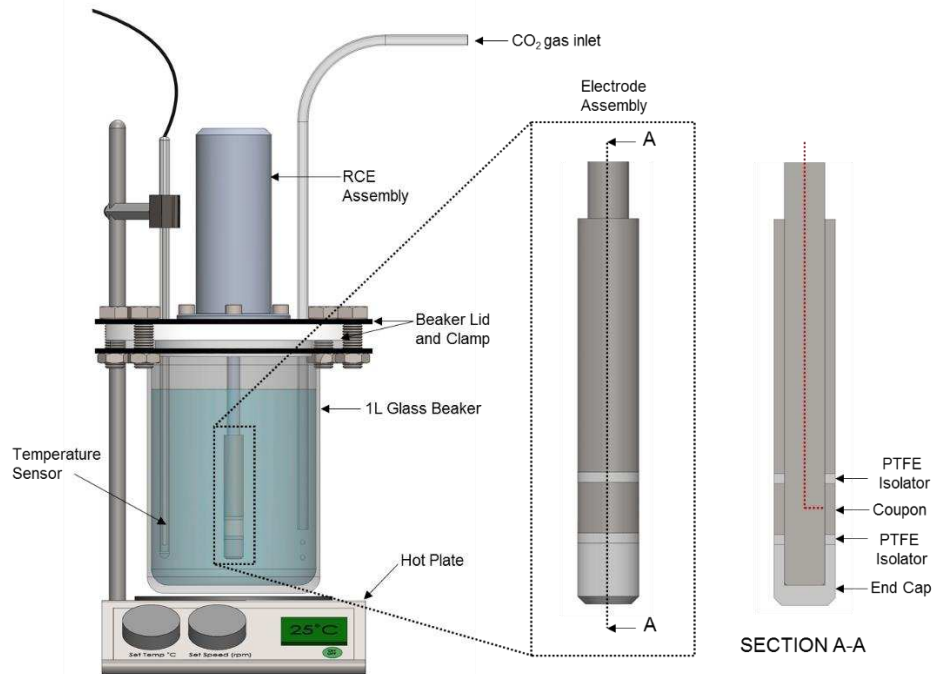


Figure 3: Schematic of RCE experimental setup used to obtain an empirical relationship between mass transfer coefficients and corrosion rates of X65 carbon steel

3. Mathematical Model

3.1. Rapid Expansion CFD Model

A CFD-enabled CO₂ corrosion model was developed by using CFD to simulate the fluid flow and the mass transport of H⁺ ions through the rapid expansion geometry, determining the mass transfer coefficients from the CFD model and integrating these into an empirical CO₂ corrosion model. The rapid expansion model is shown in Figure 4. The component was modelled assuming 2D axisymmetric conditions, to reduce computational time and to simplify the model without reduction in accuracy. A fully developed flow profile of 100 internal diameters was specified at the inlet of the rapid expansion by solving fluid flow and species transport through a straight pipe of this length with a diameter equal to the diameter prior to the expansion. The flow profile and

concentration profile at the exit of the straight pipe was specified at the inlet of the rapid expansion. An additional length of five diameters was modelled at the inlet of the rapid expansion to ensure that a fully developed flow and concentration profile was used in the calculation of mass transfer coefficients.

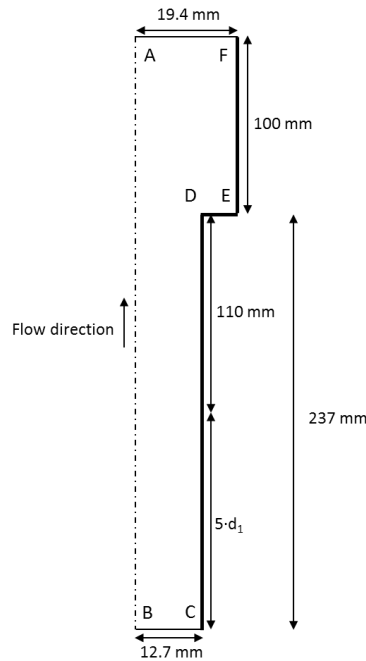


Figure 4: Geometry of the CFD rapid expansion model used to simulate fluid flow and H^+ mass transfer coefficients used for corrosion rate predictions, where d_1 is the diameter of the pipe before the expansion

3.2. Fluid Flow Model

COMSOL Multiphysics version 5.3a [36] was used to solve the CFD fluid flow and mass transport equations. COMSOL Multiphysics solves a finite element discretisation of the Navier-Stokes equations for fluid flow. Flow through the geometry was turbulent ($Re = 57,029$ for the conditions modelled), therefore, the use of Reynolds-Averaged Navier-Stokes (RANS) equations was required to model turbulence. The time-averaged continuity and momentum equations are given by Equations (9) and (10), assuming an incompressible, steady-state, iso-viscous flow with no gravity effects [37]:

$$\nabla \cdot \mathbf{U} = 0 \quad (9)$$

$$\rho(\mathbf{U} \cdot \nabla)\mathbf{U} = -\nabla p + \mu_{eff} \nabla^2 \mathbf{U} \quad (10)$$

where \mathbf{U} is the velocity vector (m/s) consisting of mean flow velocity components and turbulent fluctuation components of the flow velocity, p is the pressure (Pa) and μ_{eff} is the sum of the dynamic viscosity and μ_t , the turbulent viscosity (Pa·s), $\mu_{eff} = \mu + \mu_t$. The turbulent viscosity term is defined for the turbulence model used in the Supplementary Material.

CFD has been used to predict mass transfer coefficients in different pipe flow geometries [27, 38, 39]. It has been reported that the use of turbulence models that fully resolve the fluid flow to the wall are required to predict mass transfer coefficients in turbulent flow, due to the mass transfer boundary layer being well within the viscous sub-layer at a dimensionless wall distance of $y^+ \sim 0.1$, with wall functions not resolving to this level of accuracy [39, 40]. Therefore, a fine mesh is required adjacent to the wall to fully resolve the species transport in this region and obtain accurate mass transfer coefficients. The $k-\omega$ Shear Stress Transport (SST) turbulence model was used in this study to predict the fluid flow through the rapid expansion. The SST model combines the $k-\varepsilon$ and $k-\omega$ turbulence models, with the $k-\varepsilon$ model showing better performance in the free stream and the $k-\omega$ model more accurate in predictions in the viscous sublayer [41]. The equations used in the SST turbulence model are available in the Supplementary Material.

The $k-\omega$ turbulence model is often favoured for modelling turbulent internal pipe flow and therefore justified the use of the SST model in the rapid expansion [37]. However, to demonstrate that the SST turbulence model was appropriate, it was compared with predictions made using the low-Reynolds $k-\varepsilon$ turbulence model [42] and the Spalart-Allmaras turbulence model [43]. The SST turbulence model was most accurate when compared against the Berger and Hau [30] correlation, used to calculate mass transfer coefficients in a straight pipe of equivalent diameter and conditions to the flow characteristics prior to the rapid expansion, with a percentage difference of 4%, compared to 6% for the low-Reynolds $k-\varepsilon$ turbulence model and 15% for the Spalart-Allmaras turbulence model.

3.3. Mass Transfer Model

To determine mass transfer coefficients in the rapid expansion geometry, H^+ ions were transported through the geometry and coupled to the fluid flow model. The convection-

diffusion equation, assuming steady-state conditions and no production of H⁺ by chemical reaction, is defined as [44]:

$$N_{[H^+]} = \nabla \cdot (c_{[H^+]} \mathbf{U}) - D_{[H^+]} \nabla^2 c_{[H^+]} \quad (11)$$

Where $N_{[H^+]}$ is the flux of H⁺ (mol/m²), $D_{[H^+]}$ is the diffusion coefficient (m²/s) and $c_{[H^+]}$ is the concentration of H⁺ (mol/m³). The diffusion coefficient of H⁺ ions in water solution at a temperature of 25°C and dynamic viscosity of 8.89 x10⁻⁴ Pa·s is 9.31 x 10⁻⁹ m²/s [45]. The mass transfer coefficient is defined as Equation (12) [46]:

$$k_{m,j} = \frac{N_j}{c_{b,j} - c_{s,j}} \quad (12)$$

where $c_{b,j}$ is the concentration of the species j in the bulk solution (mol/m³) and $c_{s,j}$ is the concentration of species j at the steel surface (mol/m³). When considering the transport of H⁺ in a diffusion-controlled environment, all H⁺, by definition, is consumed at the steel surface in the cathodic reaction, Equation (1), therefore $c_{s[H^+]} = 0$ mol/m³ [14].

The flux of H⁺ ions can be determined at the steel surface using Equation (13). From this flux, the mass transfer coefficient could then be calculated.

$$N_{s[H^+]} = \mathbf{n} \cdot \nabla c_{[H^+]} \quad (13)$$

where $N_{s[H^+]}$ is the flux of H⁺ normal (\mathbf{n}) to the steel surface (mol/m²).

Equation (11) does not account for the effects of turbulence and as fluid flow through the rapid expansion was turbulent, a turbulent diffusivity term was used to account for the effects of turbulence on the transport of H⁺ ions, defined by Equation (14) [44]:

$$D_t = \frac{\mu_t}{\rho S c_t} \quad (14)$$

where D_t is the turbulent diffusivity (m²/s), μ_t is the turbulent viscosity term (Pa·s) defined for the SST turbulence model [41] and $S c_t$ is the turbulent Schmidt number. A turbulent Schmidt number of 0.5 was assumed in CFD simulations of species transport in turbulent flow. This value cannot be determined easily and is influenced by the flow geometry and the distance from a wall, but turbulent Schmidt numbers often reported are in the range of 0.5 to 0.9 [47]. It was shown that a value of 0.5 was accurate for the model developed in this paper, through comparison of CFD predictions and experimental results.

3.4. Boundary Conditions

For the fluid flow model, a flow velocity of 2 m/s was specified at the inlet of the 100 diameter straight pipe to replicate the flow-induced corrosion test conditions, assuming a fluid density, ρ , of 998 kg/m³ and dynamic viscosity, μ , of 8.89 x10⁻⁴ Pa·s, used to replicate water at a temperature of 25°C [48]. A summary of the boundary conditions used are shown in Table 2. Ambient pressure conditions were assumed at the flow inlet and outlet of the model and flow velocity was assumed to be zero at the walls, with an inlet flow velocity equal to the fully developed flow profile for a straight pipe.

Turbulence intensity of 5% and mixing length scale of 7% of the pipe diameter prior to the expansion were specified as turbulence boundary conditions at the inlet of the expansion, typical parameters for a fully developed pipe flow [37]. The turbulence model boundary conditions for the same boundaries as shown in Table 2 are given in the Supplementary Material. A systematic variation of the turbulence intensity and turbulence length scale was completed, and shown in the Supplementary Material, to demonstrate that predicted mass coefficients were not sensitive to changes in these parameters.

For the mass transfer model, the concentration of H⁺ at the walls was assumed to be 0 mol/m³ ($c_{s[H^+]} = 0$ mol/m³), simulating a scenario whereby all H⁺ that is transported to the surface is consumed. The concentration of H⁺ ions is determined from the pH of the solution and simulation of species transport in a 100 diameter straight pipe to obtain the inflow concentration profile at the rapid expansion inlet for a fully developed pipe flow. The concentration boundary conditions in the model are summarised in Table 2.

Table 2: Boundary conditions of velocity, pressure and H⁺ concentration for the boundaries as labelled in Figure 4, where \mathbf{U}_{in} is the inlet flow velocity profile for a fully developed straight pipe flow, c_{in} is the concentration profile for a fully developed straight pipe flow and \mathbf{n} is normal to the boundary

Boundary	Description	p	\mathbf{U}	$c_{[H^+]}$
AB	Symmetry axis	$\mathbf{n} \cdot \nabla p = 0$	$\mathbf{n} \cdot \nabla \mathbf{U} = 0$	$\mathbf{n} \cdot \nabla c_{[H^+]} = 0$
BC	Flow inlet	$\mathbf{n} \cdot \nabla p = 0$	$\mathbf{U} = \mathbf{U}_{in}$	$c_{[H^+]} = c_{in}$
CD, DE, EF	Pipe walls	$\mathbf{n} \cdot \nabla p = 0$	$\mathbf{U} = 0$	$c_{[H^+]} = 0$
FA	Flow outlet	$p = 0$	$\mathbf{n} \cdot \nabla \mathbf{U} = 0$	$\mathbf{n} \cdot \nabla c_{[H^+]} = 0$

3.5. CFD Model Mesh

Triangular finite elements were used for the bulk fluid flow domain and rectangular boundary elements were used adjacent to the wall, with the dimensionless distance to the centre of the elements in the first layer adjacent to the walls having a thickness of $y^+ < 0.1$, to accurately predict fluid flow and species transport in the mass transfer boundary layer, within the viscous sublayer. A mesh sensitivity study was completed to assess the influence of the number of elements in the mesh on the calculated mass transfer coefficient. The mesh sensitivity study in Figure 5 showed that the maximum predicted mass transfer coefficient after the expansion did not change significantly when more than 70,986 elements were used in the mesh. Results are shown as the percentage accuracy of the maximum mass transfer coefficient, relative to the maximum mass transfer coefficient of 0.276 mm/s, predicted using the most refined mesh, consisting of 248,552 elements. A mesh consisting of 70,986 first order elements was therefore used for fluid flow and species transport simulations in the rapid expansion, with a higher concentration of smaller elements in the region close to the wall at the expansion. Results were not sensitive to changes in the element order, with no significant improvement in accuracy, compared with experimental results, achieved with the use of second order elements.

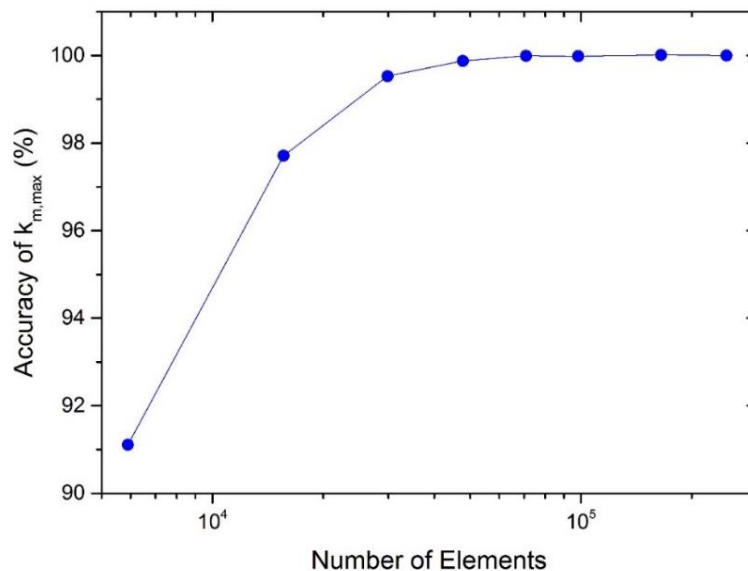


Figure 5: Mesh sensitivity study showing the maximum mass transfer coefficient ($k_{m,max}$) predicted after the expansion as a percentage accuracy compared to the maximum mass transfer coefficient (0.276 mm/s) predicted using the most refined mesh (248,552 elements)

3.6. Prediction of Carbon Steel CO₂ Corrosion Rate in the Rapid Expansion

To predict corrosion rates, RCE experiments were completed to derive an empirical relationship between mass transfer coefficient and corrosion rate, which was subsequently integrated into the CFD model to predict corrosion rates in the rapid expansion as a function of the variable mass transfer coefficient in the flow geometry. It has been previously suggested that mass transfer coefficients can be effectively used as a scaling parameter between various laboratory setups and system/sample geometries, particularly at low pH (pH < 4) [2, 46, 47].

4. Results and Discussion

4.1. CFD Prediction and Measurements of Mass Transfer Coefficients

The fluid flow through the rapid expansion at a flow velocity of 2 m/s and 25°C is shown in Figure 6, focused on the region of the rapid increase in cross-sectional area. The flow velocity decreased after the rapid expansion, with a low flow velocity region predicted immediately after the change in diameter. Recirculation of the fluid in this region was predicted, as shown by the streamlines in Figure 6.

Experimentally-measured mass transfer coefficients using the limiting current technique were compared with predictions of mass transfer coefficients from CFD. Limiting currents measured in N₂-saturated, pH 3 conditions at each of the X65 coupon locations in the rapid expansion geometries were used to determine mass transfer coefficients. The cathodic polarisation sweeps measured throughout the rapid expansion are shown in Figure 7. Limiting currents were observed between potentials of -800 mV and -1100 mV vs Ag/AgCl reference, where no increase in corrosion current density was observed despite cathodically polarising the working electrode, indicating a limiting current. The limiting current was obtained by determining the average current between -900 mV and -1000 mV for the coupons positioned at 116 mm, 119 mm and 122 mm where lower mass transfer coefficients were measured. For all other coupons, the limiting current was obtained between -1000 mV and -1100 mV. The maximum variation in the current measured for all coupons in the potential range was less than ±10%, relative to the average values used as limiting currents.

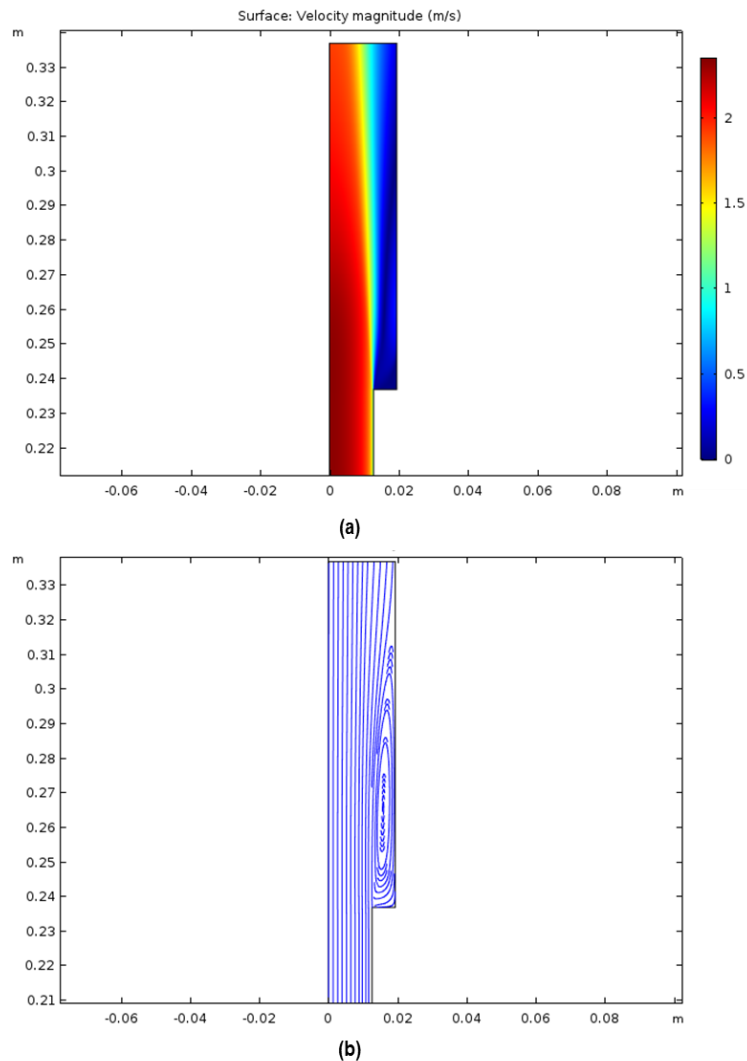


Figure 6: Prediction of fluid flow in the rapid expansion, showing (a) flow velocity and (b) fluid flow streamlines at a mean inlet flow velocity of 2 m/s and solution temperature of 25°C

Limiting current measurements were subsequently used to calculate mass transfer coefficients using Equation (7) and are compared with the CFD model-predicted mass transfer coefficients in Figure 8 in the rapid expansion. The average limiting current from two measurements is plotted in Figure 8, with error bars in the y-axis representing the variation in the limiting current values determined from Figure 7 and the accuracy of pH measurements (assumed to be accurate to $\text{pH} \pm 0.05$, accounting for probe resolution and calibration accuracy), resulting in error in the calculation of mass transfer coefficient using Equation (7). Experimental mass transfer coefficients are shown as points in Figure 8, reported as the distance from the inlet of the expansion to the centre of the X65 coupons. Electrochemical measurements produce limiting currents averaged over the

surface area of the coupons, potentially leading to some discrepancy between measured and predicted mass transfer coefficients after the expansion at the points shown, where mass transfer coefficients are not constant across the surface area of a coupon. Error bars in the x-axis represent the diameter of the coupons.

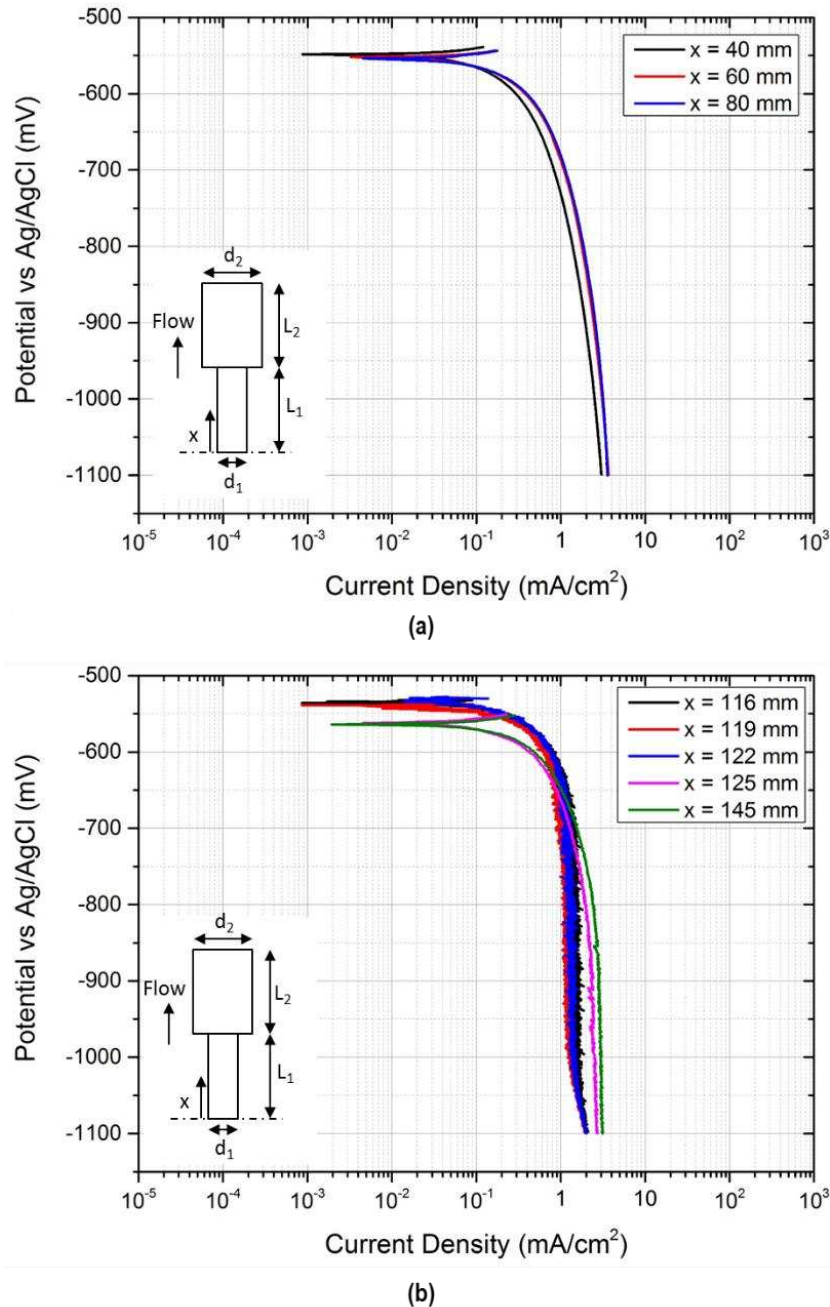


Figure 7: Cathodic polarisation sweeps in a N₂-saturated, pH 3, 2 wt.% NaCl conditions measured on the X65 coupons, (a) before the expansion and (b) after the expansion, indicating a limiting current, where d₁ = 25.4 mm, d₂ = 38.8 mm, L₁ = 110 mm, L₂ = 100 mm and x is the distance to the centre of the coupons from the inlet of the expansion

CFD predictions showed that mass transfer coefficients decreased significantly immediately after the rapid expansion, compared to the mass transfer coefficients prior to the expansion, before increasing gradually towards the exit of the expansion. The mass transfer coefficient reported at 110 mm is the predicted mass transfer coefficient at the start of the pipe wall after the expansion. Good agreement was observed prior to the expansion between mass transfer coefficients predicted using CFD and mass transfer coefficients predicted using the Berger and Hau [30] correlation, applicable in straight pipes. The difference between the mass transfer coefficients calculated using Equation (4) and CFD predictions was 3.9%. This equation, however, cannot be applied to predict mass transfer coefficients immediately after the expansion. The CFD model predictions after the expansion showed a similar trend to the results reported by Rizk et al. [26], giving confidence in the predictions before and after the expansion. They measured mass transfer coefficients approximately 1.5 times greater at coupons located 1.5 diameters (relative to the larger diameter after the expansion, d_2) downstream of an expansion compared to coupons located 0.5 diameters after the expansion. The maximum CFD-predicted mass transfer coefficient in Figure 8 was approximately 1.3 times greater than the mass transfer coefficient 0.5 diameters after the expansion.

Good agreement was observed between the experimentally-determined mass transfer coefficients from limiting currents and CFD predictions in Figure 8. The most significant difference between experimental results and numerical predictions exists immediately after the expansion, where recirculation of the fluid resulted in a significant decrease and fluctuation in the predicted mass transfer coefficient. Experimental validation was completed in this region, however, due to the coupon size, electrochemically-measured average mass transfer coefficients would have been influenced by the significant variation in flow conditions across the surface area of the coupon, explaining some discrepancy between experimental and predicted mass transfer coefficients in this region. However, a clear and significant drop in mass transfer coefficients was measured immediately after the expansion, validating the trend predicted using CFD. This trend would not have been accurately predicted using a model such as the Berger and Hau [30] model, where only a constant mass transfer coefficient can be obtained across a uniform diameter straight pipe.

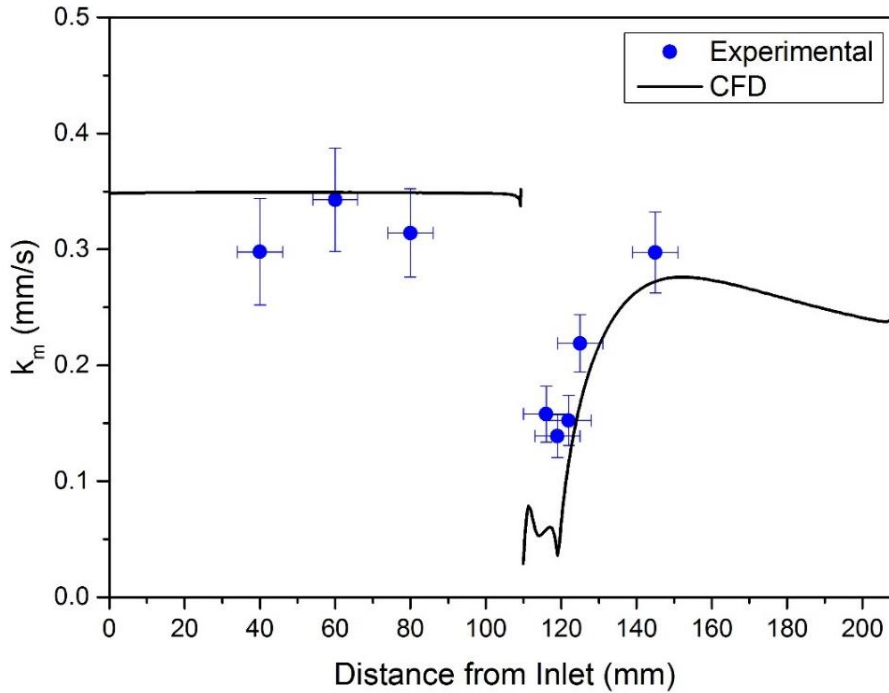


Figure 8: Comparison of experimentally-determined mass transfer coefficients of H^+ from limiting current measurements at a flow velocity of 2 m/s and solution temperature of 25°C in a pH 3 solution with CFD predictions of mass transfer coefficients in the rapid expansion at a flow velocity of 2 m/s and solution temperature of 25°C

4.2. Empirical CO_2 Corrosion Rate Model

The RCE was used to obtain a simple empirical relationship between mass transfer coefficient and corrosion rate. The corrosion rates, measured from 4 h mass loss tests, are shown in Figure 9. Error bars in Figure 9 represent the maximum and minimum corrosion rates measured from a minimum of two experiments. A logarithmic relationship between mass transfer coefficient and corrosion rate was observed, and produced a similar trend to that observed in similar low pH conditions reported by other authors [17, 18]. The logarithmic relationship, Equation (15), was determined to enable corrosion rates in mm/yr (V_c) to be predicted as a function of mass transfer coefficients in m/s, which was integrated into the CFD simulations of species transport in the rapid expansion to predict corrosion rates.

$$V_c = 3.54 \ln(k_m + 8.17 \times 10^{-5}) + 32.7 \quad (15)$$

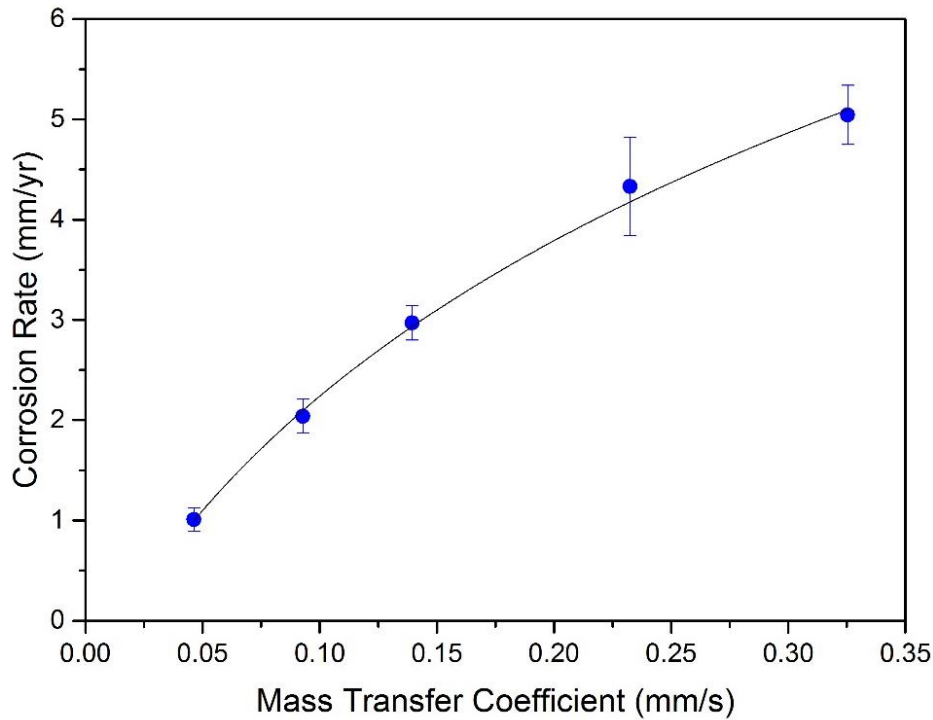


Figure 9: Effect of mass transfer coefficients on corrosion rates determined from gravimetric measurements of X65 carbon steel in 4 h RCE experiments in a CO₂-saturated, 2% NaCl, pH 3.7 solution at a temperature of 25°C

4.3. Prediction and Measurements of Corrosion Rates

Corrosion rates in the rapid expansion with a 2% NaCl, CO₂-saturated, pH 3.7 solution were predicted using the CFD-enabled corrosion model detailed above. Corrosion rates of the X65 coupons in the rapid expansion were obtained using mass loss measurements of the coupons after corrosion tests. To demonstrate that corrosion rates determined from mass loss were representative of corrosion rates throughout the 4 h test period, electrochemical measurements were completed to determine polarisation resistance, R_p , of the coupons during the test, shown as $1/R_p$ in Figure 10. Results were obtained for rapid expansion 1 (as described in Section 2.1) from the average of three measurements, with the standard deviation reported. This showed that corrosion rates would remain constant throughout the 4 h test duration, proving that mass loss results gave an accurate representation of the corrosion rates during a test.

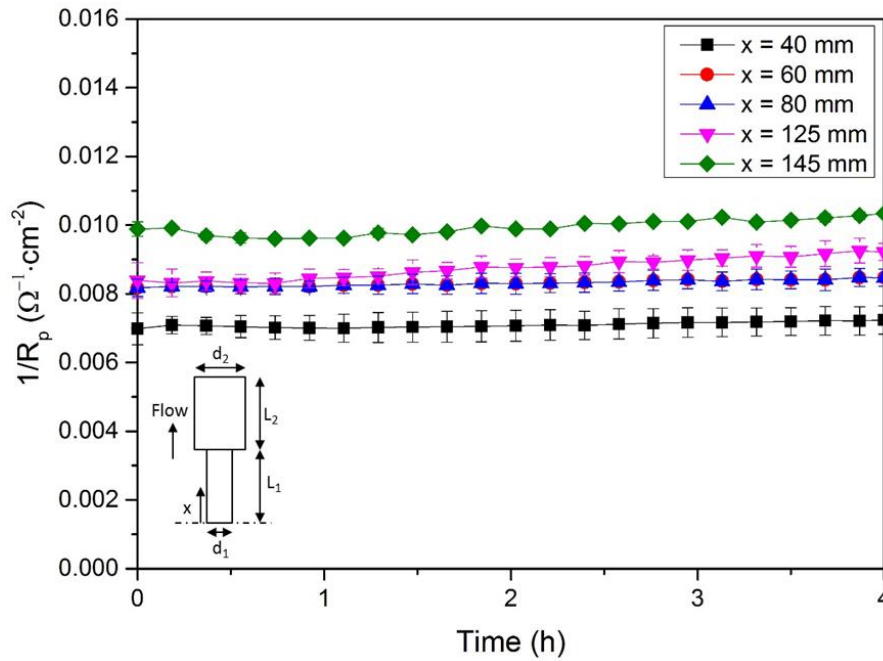


Figure 10: Polarisation resistances (not corrected for solution resistance) of X65 coupons in the rapid expansion during 4 h tests at a flow velocity of 2 m/s in a 25°C, CO₂-saturated, pH 3.7 solution, where $d_1 = 25.4$ mm, $d_2 = 38.8$ mm, $L_1 = 110$ mm, $L_2 = 100$ mm and x is the distance to the centre of the coupons from the inlet of the expansion, showing constant polarisation resistances over time

The CFD-enabled corrosion modelling approach was used to predict corrosion rates on the surface of the rapid expansion component. The predicted corrosion rates on the surfaces of the rapid expansion component are shown at 2 m/s and 25°C in Figure 11, mapped onto a 3D geometry assuming axisymmetric conditions. Mass transfer coefficients were used as the input in the corrosion rate numerical model and predicted throughout the geometry. The mathematical model predicted that the corrosion rate decreased immediately after the rapid expansion and gradually increased towards the component outlet. Corrosion rates after the expansion were lower than corrosion rates prior to the expansion.

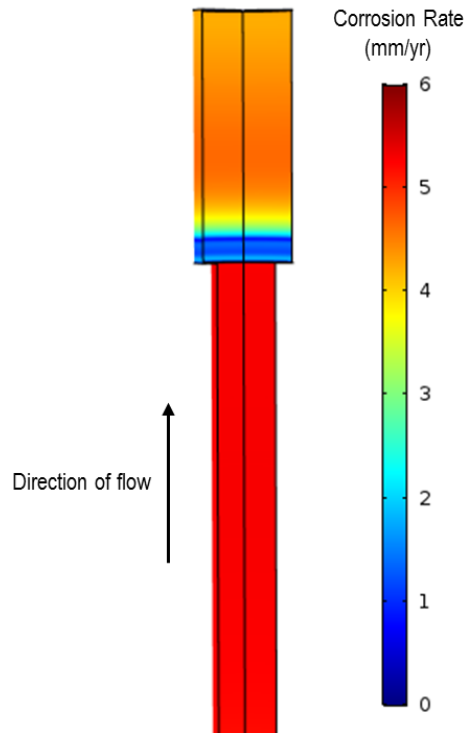


Figure 11: Corrosion rate predictions using CFD and an empirical model on the internal surface of a carbon steel rapid expansion pipe subject to a CO₂-saturated, 2 wt.% NaCl, pH 3.7, 25°C solution flowing through the expansion at a flow velocity of 2 m/s

When comparing numerical and experimental corrosion rates of X65 carbon steel in the rapid expansion, higher corrosion rates were also measured before the expansion and decreased after the expansion, Figure 12. Average corrosion rates are reported from two measurements, with the error bars in the y-axis representing the maximum and minimum corrosion rates measured. Error bars shown in the x-axis represent the diameter of the coupons. The average difference between the corrosion rates measured experimentally and the corrosion rates predicted from the combined CFD and empirical model was <4% (predicted corrosion rates were averaged over a distance equivalent to the diameter of the coupons). Significantly lower corrosion rates were measured immediately after the rapid expansion, experimentally validating the predicted corrosion rates in this region and demonstrating the necessity for accurate mass transfer coefficient predictions. The application of a corrosion model which uses a single mass transfer coefficient input would not have predicted accurate corrosion rates in this region.

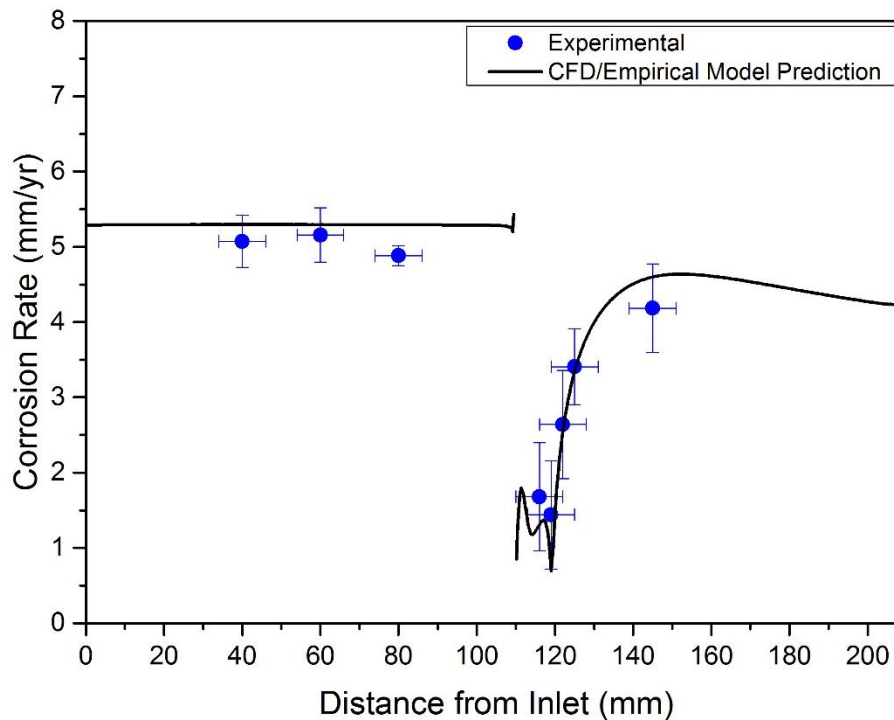


Figure 12: Comparison of corrosion rates determined from CFD-predicted mass transfer coefficients of H^+ input into a mechanistic CO_2 corrosion model, with experimentally-measured corrosion rates in a CO_2 -saturated, 2% NaCl, pH 3.7 solution in the rapid expansion at a temperature of 25°C and flow velocity of 2 m/s, determined from gravimetric measurements

4.4. Potential Application of Methodology in the Field and Other Complex Geometries

This study has demonstrated the necessity for use of the computationally efficient method of obtaining mass transfer coefficients of H^+ from CFD predictions to predict corrosion rates using a CO_2 corrosion model. Definition of fluid flow parameters is challenging in a complex flow geometry, as knowledge of the flow velocity or determination of another basic flow parameter does not fully characterise the hydrodynamic conditions. As demonstrated in Figure 8 and Figure 12, a significant decrease in mass transfer coefficients and corrosion rates, respectively, was predicted and measured after the rapid expansion, which would not have been easily determined without the application of CFD. Other complex pipe geometries, such as rapid contractions and elbows, have also shown changes in corrosion rates after a flow disturbance [28, 33].

Significant potential exists to apply this methodology for CO_2 corrosion predictions in other complex flow geometries. It has been demonstrated in this study and by several

others [2, 23, 24] that mass transfer coefficients strongly relate hydrodynamic conditions to corrosion rates when $\text{pH} < 4$. Silverman [23, 24] and Nešić et al. [2] also showed that mass transfer coefficients can be used to translate flow-induced CO_2 corrosion conditions at $\text{pH} < 4$ between different flow environments, showing strong agreement between corrosion rates measured in different geometries, such as a straight pipe and RCE, when mass transfer coefficients were reproduced in the different environments. Therefore, the methodology used in this study further demonstrates the significant potential for highly accurate predictions of CO_2 corrosion rates across a range of different geometries in low pH conditions, where corrosion rates are strongly related to the mass transfer coefficients.

Whilst a simple empirical model was used in this study, mechanistic models, such as those developed by Zheng et al. [18] and Al-Khateeb et al. [17], rely on inputs of mass transfer coefficients to predict CO_2 corrosion rates and are, therefore, limited by the availability of readily-determined mass transfer coefficients in a particular geometry of interest. Whilst this is possible for simple flow geometries, such as straight pipes or RCEs, applying these models in more complex geometries could result in under or over prediction of corrosion rates, potentially resulting in significant consequences for pipeline design and management in the field, which CO_2 corrosion prediction tools are often used for. Therefore, integrating a mathematical model into CFD predictions of mass transfer coefficients to predict corrosion rates in complex geometries, widens the potential usage of mechanistic CO_2 corrosion models.

5. Conclusions

Flow-induced corrosion rates of X65 carbon steel were predicted and determined experimentally in a rapid expansion component to validate use of a new CFD-enabled empirical CO_2 corrosion correlation to predict corrosion rates in a complex flow geometry. This work demonstrates the necessity for using CFD predictions of mass transfer to extend the application of existing CO_2 corrosion models and/or correlations, developed and validated for simple flow geometries, such as a straight pipe and a RCE, into more complex flow geometries, representative of flow geometries that would be typical in the field. The following conclusions were reached:

- A new CFD-enabled CO₂ corrosion modelling methodology was used to successfully predict the mass transfer coefficients and corrosion rates in a rapid expansion geometry, demonstrating the potential for application of CO₂ corrosion models/correlations in a complex flow geometry with local variations in mass transfer coefficients
- CFD was used to accurately predict local mass transfer coefficients in the rapid expansion using an SST turbulence model, validated against other studies and showing a good agreement between experimentally-measured mass transfer coefficients determined using an electrochemical limiting current technique and CFD predictions
- Lower mass transfer coefficients, and hence corrosion rates, were observed immediately after the rapid expansion, before increasing towards the exit of the rapid expansion, demonstrating how simple flow parameters did not fully represent flow-induced CO₂ corrosion in these conditions, potentially leading to an over-prediction of corrosion rates without the application of CFD
- Corrosion rates were predicted in a rapid expansion geometry at a flow velocity of 2 m/s and solution temperature of 25°C showing accurate predictions in the conditions modelled, with a difference of <4% between experimentally measured corrosion rates and predicted corrosion rates.

Acknowledgements

The authors would like to thank EPSRC and Shell UK for the funding of this research. The authors would also like to thank Michael Huggan and Graham Brown in the School of Mechanical Engineering at University of Leeds for their expertise and assistance in the design and manufacture of the rapid expansion component.

Data Availability

The raw/processed data required to reproduce these findings cannot be shared at this time as the data also forms part of an ongoing study.

References

1. Nešić, S., *Key issues related to modelling of internal corrosion of oil and gas pipelines – A review*. Corrosion Science, 2007. **49**(12): p. 4308-4338.
2. Nešić, S., Solvi, G.T., and Enerhaug, J., *Comparison of the Rotating Cylinder and Pipe Flow Tests for Flow-Sensitive Carbon Dioxide Corrosion*. Corrosion, 1995. **51**(10): p. 773-787.
3. Efird, K., Wright, E., Boros, J., and Hailey, T., *Correlation of steel corrosion in pipe flow with jet impingement and rotating cylinder tests*. Corrosion, 1993. **49**(12): p. 992-1003.
4. Efird, K.D., *Jet impingement testing for flow accelerated corrosion*, in *CORROSION 2000*. 2000, NACE International: Orlando, FL.
5. Efird, K.D., *Flow accelerated corrosion testing basics*, in *CORROSION 2006*. 2006, NACE International: San Diego, CA.
6. Gulbrandsen, E. and Grana, A., *Testing of Carbon Dioxide Corrosion Inhibitor Performance at High Flow Velocities in Jet Impingement Geometry. Effects of Mass Transfer and Flow Forces*. CORROSION, 2007. **63**(11): p. 1009-1020.
7. De Waard, C. and Milliams, D.E., *Carbonic Acid Corrosion of Steel*. Corrosion, 1975. **31**(5): p. 177-181.
8. Linter, B. and Burstein, G., *Reactions of pipeline steels in carbon dioxide solutions*. Corrosion science, 1999. **41**(1): p. 117-139.
9. Remita, E., Tribollet, B., Sutter, E., Vivier, V., Ropital, F., and Kittel, J., *Hydrogen evolution in aqueous solutions containing dissolved CO₂: Quantitative contribution of the buffering effect*. Corrosion Science, 2008. **50**(5): p. 1433-1440.
10. Kahyarian, A., Brown, B., and Nešić, S., *Electrochemistry of CO₂ corrosion of mild steel: Effect of CO₂ on cathodic currents*. Corrosion, 2018. **74**(8): p. 851-859.
11. Tran, T., Brown, B., and Nestic, S., *Corrosion of mild steel in an aqueous CO₂ environment - basic electrochemical mechanisms revisited*, in *CORROSION 2015*. 2015, NACE International: Dallas, TX.
12. Kahyarian, A. and Nestic, S., *A New Narrative for CO₂ Corrosion of Mild Steel*. Journal of The Electrochemical Society, 2019. **166**(11): p. C3048-C3063.
13. das Chagas Almeida, T., Bandeira, M.C., Moreira, R.M., and Mattos, O.R. *The role of CO₂ on carbon steel corrosion*. in *CORROSION 2015*. 2015. Dallas, TX: NACE International.
14. Sydberger, T. and Lotz, U., *Relation between mass transfer and corrosion in a turbulent pipe flow*. Journal of the Electrochemical Society, 1982. **129**(2): p. 276-283.
15. Barker, R., Burkle, D., Charpentier, T., Thompson, H., and Neville, A., *A review of iron carbonate (FeCO₃) formation in the oil and gas industry*. Corrosion Science, 2018.
16. Barker, R., Hua, Y., and Neville, A., *Internal corrosion of carbon steel pipelines for dense-phase CO₂ transport in carbon capture and storage (CCS)—a review*. International Materials Reviews, 2017. **62**(1): p. 1-31.
17. Al-Khateeb, M., Barker, R., Neville, A., and Thompson, H., *An experimental and theoretical investigation of the influence of surface roughness on corrosion in CO₂ environments*. Journal of Corrosion Science and Engineering, 2018. **20**.
18. Zheng, Y., Ning, J., Brown, B., and Nešić, S., *Advancement in predictive modeling of mild steel corrosion in CO₂-and H₂S-containing environments*. Corrosion, 2016. **72**(5): p. 679-691.

19. Bockris, J.M., Drazic, D., and Despic, A., *The electrode kinetics of the deposition and dissolution of iron*. *Electrochimica Acta*, 1961. **4**(2-4): p. 325-361.
20. Halvorsen, A.M. and Sontvedt, T., *CO₂ Corrosion Model for Carbon Steel Including Wall Shear Stress Model for Multiphase Flow and Limits for Production Rate to Avoid Mesa Attack*, in *CORROSION 99*. 1999, NACE International: San Antonio, TX.
21. Poulson, B., *Advances in understanding hydrodynamic effects on corrosion*. *Corrosion Science*, 1993. **35**(1-4): p. 655-665.
22. Nestic, S., Postlethwaite, J., and Olsen, S., *An electrochemical model for prediction of corrosion of mild steel in aqueous carbon dioxide solutions*. *Corrosion*, 1996. **52**(4): p. 280-294.
23. Silverman, D., *The rotating cylinder electrode for examining velocity-sensitive corrosion-a review*. *CORROSION*, 2004. **60**(11): p. 1003-1023.
24. Silverman, D.C., *Rotating Cylinder Electrode - Geometry Relationships for Prediction of Velocity-Sensitive Corrosion*. *CORROSION*, 1988. **44**(1): p. 42-49.
25. Kahyarian, A., Singer, M., and Nestic, S., *Modeling of uniform CO₂ corrosion of mild steel in gas transportation systems: A review*. *Journal of Natural Gas Science and Engineering*, 2016. **29**: p. 530-549.
26. Rizk, T., Thompson, G., and Dawson, J., *Mass transfer enhancement associated with sudden flow expansion*. *Corrosion Science*, 1996. **38**(10): p. 1801-1814.
27. Wang, J., Shirazi, S., Shadley, J., Rybicki, E., and Dayalan, E., *A correlation for mass transfer coefficients in elbows*, in *CORROSION 98*. 1998, NACE International: San Diego, CA.
28. Malka, R., Nešić, S., and Gulino, D.A., *Erosion–corrosion and synergistic effects in disturbed liquid-particle flow*. *Wear*, 2007. **262**(7–8): p. 791-799.
29. El-Gammal, M., Mazhar, H., Cotton, J.S., Shefski, C., Pietralik, J., and Ching, C.Y., *The hydrodynamic effects of single-phase flow on flow accelerated corrosion in a 90-degree elbow*. *Nuclear Engineering and Design*, 2010. **240**(6): p. 1589-1598.
30. Berger, F.P. and Hau, K.F.F.L., *Mass transfer in turbulent pipe flow measured by the electrochemical method*. *International Journal of Heat and Mass Transfer*, 1977. **20**(11): p. 1185-1194.
31. Eisenberg, M., Tobias, C., and Wilke, C., *Ionic mass transfer and concentration polarization at rotating electrodes*. *Journal of the Electrochemical Society*, 1954. **101**(6): p. 306-320.
32. Al-Khateeb, M., Barker, R., Neville, A., and Thompson, H.M., *The effect of surface roughness on diffusion and chemical reaction controlled limiting currents on a Rotating Cylinder Electrode in deaerated solutions with and without CO₂*. *CORROSION*, 2018. **74**(9): p. 971-983.
33. Owen, J., Ducker, E., Huggan, M., Ramsey, C., Neville, A., and Barker, R., *Design of an elbow for integrated gravimetric, electrochemical and acoustic emission measurements in erosion-corrosion pipe flow environments*. *Wear*, 2019. **428-429**: p. 76-84.
34. Yunus, A.C. and Cimballa, J.M., *Fluid mechanics fundamentals and applications*. McGraw-Hill. 2006, Boston.
35. Owen, J., Ramsey, C., Barker, R., and Neville, A., *Erosion-corrosion interactions of X65 carbon steel in aqueous CO₂ environments*. *Wear*, 2018. **414-415**: p. 376-389.

36. COMSOL Multiphysics v5.3a Chemical Reaction Engineering Module User's Guide. 2017.
37. Versteeg, H.K. and Malalasekera, W., *An introduction to computational fluid dynamics: the finite volume method*. 2007, Harlow: Pearson Education.
38. Nešić, S. and Postlethwaite, J., *Hydrodynamics of disturbed flow and erosion-corrosion. Part I - Single-phase flow study*. The Canadian Journal of Chemical Engineering, 1991. **69**(3): p. 698-703.
39. Srinivasan, V., *Evaluation of Flow Coupled CO₂ Corrosion Using CFD: Kinetics & Hydrodynamics*, in *CORROSION 2015*. 2015, NACE International: Dallas, TX.
40. Nešić, S., Postlethwaite, J., and Bergstrom, D.J., *Calculation of wall-mass transfer rates in separated aqueous flow using a low Reynolds number κ - ϵ model*. International Journal of Heat and Mass Transfer, 1992. **35**(8): p. 1977-1985.
41. Menter, F.R., *Review of the shear-stress transport turbulence model experience from an industrial perspective*. International Journal of Computational Fluid Dynamics, 2009. **23**(4): p. 305-316.
42. Abe, K., Kondoh, T., and Nagano, Y., *A new turbulence model for predicting fluid flow and heat transfer in separating and reattaching flows—I. Flow field calculations*. International journal of heat and mass transfer, 1994. **37**(1): p. 139-151.
43. Spalart, P. and Allmaras, S. *A one-equation turbulence model for aerodynamic flows*. in *30th aerospace sciences meeting and exhibit*. 1992.
44. Byron Bird, R., Warren E. Stewart, and Lightfoot, E.N., *Transport phenomena*. 2nd ed. 2007, Chichester John Wiley & Sons.
45. Atkins, P., De Paula, J., and Keeler, J., *Atkins' physical chemistry*. 9th ed. 2010, Oxford: Oxford University Press.
46. Cussler, E.L., *Diffusion: mass transfer in fluid systems*. 1984, Cambridge: Cambridge University Press.
47. Tominaga, Y. and Stathopoulos, T., *Turbulent Schmidt numbers for CFD analysis with various types of flowfield*. Atmospheric Environment, 2007. **41**(37): p. 8091-8099.
48. Douglas, J.F., Gasiorek, J.M., Swaffield, J.A., and Jack, L.B., *Fluid Mechanics*. 5th ed. 2005, Harlow: Pearson/Prentice Hall.

An experimental and numerical investigation of CO₂ corrosion in a rapid expansion pipe geometry

Joshua Owen^a, Jack Godfrey^a, Wenlong Ma^a, Greg de Boer^a, Mohammed Al-Khateeb^a, Harvey Thompson^a, Anne Neville^a, Callum Ramsey^b and Richard Barker^a

^a School of Mechanical Engineering, University of Leeds, Leeds, LS2 9JT, United Kingdom

^b Shell U.K. Limited, 1 Altens Farm Road, Nigg, Aberdeen, AB12 3FY, United Kingdom

SUPPLEMENTARY MATERIAL

Appendix A – SST Turbulence Model

The equations used in the SST turbulence model, solved to model turbulent flow through the rapid expansion, are defined as follows, assuming an incompressible, steady-state, iso-viscous flow with no gravity effects:

$$\rho(\mathbf{U} \cdot \nabla)k = \nabla \cdot [(\mu + \sigma_k \mu_t) \nabla k] + P - \rho \beta_0^* k \omega \quad (\text{A.1})$$

$$\rho(\mathbf{U} \cdot \nabla)\omega = \nabla \cdot [(\mu + \sigma_\omega \mu_t) \nabla \omega] + \frac{\alpha}{\mu_t} \rho P - \rho \beta \omega^2 + 2(1 - f_1) \frac{\rho \sigma_{\omega 2}}{\omega} \nabla \omega \cdot \nabla k \quad (\text{A.2})$$

The turbulent viscosity (Pa·s) is given by:

$$\mu_t = \frac{\rho a_1 k}{\max(a_1 \omega, S f_2)} \quad (\text{A.3})$$

where S is the characteristic magnitude of the mean velocity gradients:

$$S = \frac{1}{2} [(\nabla \mathbf{U}) + (\nabla \mathbf{U})^T] \quad (\text{A.4})$$

The SST turbulence model uses a limiter for the production of turbulent kinetic energy, P , defined as:

$$P = \min(P_k, 10 \rho \beta_0^* k \omega) \quad (\text{A.5})$$

where P_k is the production of turbulent kinetic energy:

$$P_k = \mu_t [\nabla \mathbf{U} : \{(\nabla \mathbf{U}) + (\nabla \mathbf{U})^T\}] \quad (\text{A.6})$$

The blending function, f_i , is defined as:

$$f_1 = \tanh \left(\left\{ \min \left[\max \left(\frac{\sqrt{k}}{\beta_0^* \omega l_w}, \frac{500\mu}{l_w^2 \omega} \right), \frac{4\rho\sigma_{\omega_2} k}{CD_{k\omega} l_w^2} \right] \right\}^4 \right) \quad (\text{A.6})$$

where $CD_{k\omega}$ is defined as:

$$CD_{k\omega} = \max \left(\frac{2\rho\sigma_{\omega_2}}{\omega} \nabla\omega \cdot \nabla k, 10^{-10} \right) \quad (\text{A.7})$$

The distance to the nearest wall, l_w (m), is defined as:

$$l_w = \frac{1}{G} - \frac{l_{ref}}{2} \quad (\text{A.8})$$

where l_{ref} is reference length scale equivalent to one tenth of the shortest side of the geometry bounding box and G is the reciprocal wall distance (1/m):

$$\nabla G \cdot \nabla G + \sigma_w G (\nabla \cdot \nabla G) = (1 + 2\sigma_w) G^4 \quad (\text{A.9})$$

A second blending function, f_2 , is defined as:

$$f_2 = \tanh \left(\left[\max \left\{ \frac{2\sqrt{k}}{\beta_0^* \omega l_w}, \frac{500\mu}{\rho l_w^2 \omega} \right\} \right]^2 \right) \quad (\text{A.10})$$

The constants used in the SST model are computed using the blending functions with the corresponding constants used in the k - ε and k - ω turbulence models:

$$\phi = \phi_1 f_1 + \phi_2 (1 - f_2) \quad (\text{A.11})$$

where ϕ is a constant equivalent to α , β , σ_k and σ_ω . These constants are defined as $\alpha_1 = 5/9$, $\alpha_2 = 0.44$, $\beta_1 = 3/40$, $\beta_2 = 0.0828$, $\sigma_{k1} = 0.85$, $\sigma_{k2} = 1$, $\sigma_{\omega 1} = 0.5$ and $\sigma_{\omega 2} = 0.856$. The other constants used in the SST turbulence model equations are $\alpha_1 = 0.31$, $\beta_0^* = 0.09$ and $\sigma_w = 0.2$.

Appendix B – Turbulence Boundary Conditions

The turbulence boundary conditions are shown in Table B.1, defining the conditions at the inlet, outlet, symmetry axis and walls for turbulent kinetic energy, specific turbulence dissipation rate and the reciprocal wall distance. The boundaries are labelled as the boundaries highlighted on the model diagram shown in Figure 3.

Table B.1: Boundary conditions of turbulent kinetic energy, specific turbulent dissipation rate and reciprocal wall distance for the boundaries as labelled in Figure 3, where I_T is the turbulence intensity and L_T is the turbulence length scale

Boundary	Description	k	ω	G
AB	Symmetry axis	$\mathbf{n} \cdot \nabla k = 0$	$\mathbf{n} \cdot \nabla \omega = 0$	$\mathbf{n} \cdot \nabla G = 0$
BC	Flow inlet	$k = \frac{3}{2} (\mathbf{U}_{in} I_T)^2$	$\omega = \frac{\sqrt{k}}{(\beta_0^*)^{1/4} L_T}$	$\mathbf{n} \cdot \nabla G = 0$
CD, DE, EF	Pipe walls	$\mathbf{n} \cdot \nabla k = 0$	$\lim_{l_w \rightarrow 0} \omega = \frac{6\mu}{\rho \beta_1 l_w^2}$	$\frac{1}{G} = 0$
FA	Flow outlet	$\mathbf{n} \cdot \nabla k = 0$	$\mathbf{n} \cdot \nabla \omega = 0$	$\mathbf{n} \cdot \nabla G = 0$

Appendix C – Turbulence Intensity and Turbulent Length Scale

Analysis of the sensitivity of the predicted mass transfer coefficients to changes in the turbulence intensity and turbulence length scale was completed to demonstrate that results were not significantly influenced by changes in these parameters. Figure C.1 showed less than 2% difference was observed between the maximum mass transfer coefficient prediction after the rapid expansion compared to predictions using a turbulence intensity of 5% and mixing length scale of 7% of the pipe diameter for all combinations of turbulence boundary conditions (between 5% and 10%). A turbulence intensity of 5% and turbulence length scale of 7% of inner pipe diameter prior to the rapid expansion was chosen, giving a maximum mass transfer coefficient of 0.276 mm/s.

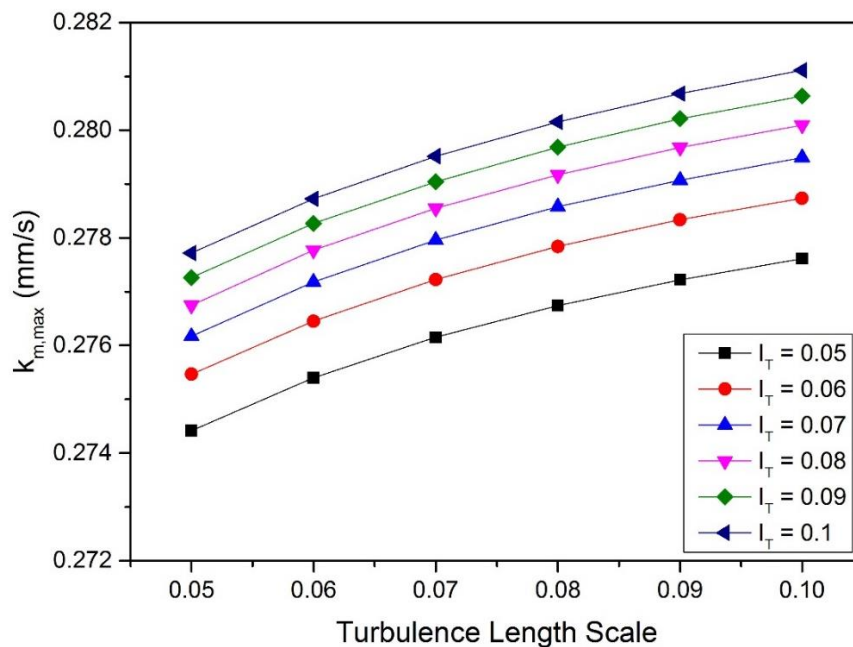


Figure C.1: Sensitivity of the maximum predicted mass transfer coefficient ($k_{m,max}$) after the expansion to changes in the inlet turbulence intensity (I_T) and turbulent length scale boundary conditions